A comparative study of dust grain polarization efficiencies in the interstellar and intracluster mediums towards anticentre galaxy

N. Bijas,[1,2]★ Chakali Eswaraiah,[1]★ Panigrahy Sandhyarani,[1] Jessy Jose[1] and Maheswar Gopinathan[3]

[1]*Indian Institute of Science Education and Research Tirupati, Rami Reddy Nagar, Karakambadi Road, Mangalam (PO), Tirupati 517507, India.*
[2]*Jodrell Bank Centre for Astrophysics, School of Physics and Astronomy, University of Manchester, Oxford Road, Manchester, M13 9PL, UK.*
[3]*Indian Institute of Astrophysics, Sarjapur Road, Koramangala, Bangalore 560034, India*

ABSTRACT

Dust polarization observations at optical wavelengths help understand the dust grain properties and trace the plane-of-the-sky component of the magnetic field. In this study, we make use of published optical polarization data acquired with AIMPOL along with distances (d) and extinction (A_V) data. We study the variation of polarization efficiency (P/A_V) as a function of A_V in the diffuse interstellar medium (ISM) and intracluster mediums (ICM) using the already published polarization data of six clusters. Among these clusters, NGC 2281, NGC 1664, and NGC 1960 are old; while Stock 8, NGC 1931, and NGC 1893 are young. We categorize stars towards each cluster into foreground, background, and cluster members by employing two clustering algorithms GMM and DBSCAN. Thus, classified field stars and cluster members are used to reveal the polarization properties of ISM and ICM dust, respectively. We find that the dust grains located in the diffuse ISM show higher polarization efficiencies when compared to those located in the ICM of younger clusters.

Key words: polarization – dust, extinction – ISM: magnetic fields.

1 INTRODUCTION

Dust grains in the interstellar medium (ISM) have been known to be responsible for the observed polarization of the background starlight. When starlight passes through the helical asymmetrically shaped dust grains in the ISM aligned with respect to the Galactic magnetic field, it undergoes differential extinction, which results in the polarization of the transmitted light (Hiltner 1949). Observation of this polarized light can yield the fraction of polarization (P), which is an important parameter that can be used to study some key dust properties (Davis & Greenstein 1951; Lazarian & Hoang 2007) apart from the plane-of-the-sky component of the magnetic field, i.e. polarization angle (PA). Two such important properties are polarization efficiency (P/A_V) and rate of polarization (P/d), which can reveal the dust alignment efficiency and the distribution of the polarizing dust grains, respectively, along a particular line-of-sight (LOS). The study of these properties has become crucial in revealing the presence of dust populations with different properties like polarization efficiency, rate of polarization, dust grain shape, size, composition, magnetic field orientation, etc., along a LOS (Bijas et al. 2022).

To understand how the dust grains with different ranges of extinction values contribute to this observed polarization, several studies have tried to analyse the variation of P/A_V as a function of extinction (A_V) by means of a power-law fit of the form $P/A_V \propto A_V^{-\alpha}$, where

the power-law index α indicates the dust grain alignment efficiency at different dust layers (Goodman et al. 1995; Chapman et al. 2011; Alves et al. 2014; Cashman & Clemens 2014; Jones et al. 2014). Typically, the values that α can take ranges from -1 to -0.5 (Goodman et al. 1992; Gerakines, Whittet & Lazarian 1995). While an index of $\alpha = 0$ indicates the perfect alignment of dust grains with the magnetic field in the region, $\alpha = -1$ indicates the poor alignment of dust grains (see Whittet et al. 2008; Pattle et al. 2019). Since the alignment of the ISM dust grains with the magnetic fields is a pre-requisite for using the dust polarization to trace the plane of the sky (POS) magnetic field orientations, the polarization efficiency of dust grains in a region is a crucial indicator to understand if the dust polarization technique can be used to trace the magnetic field morphology in a specific region of interest.

Similarly, the polarization rate (P/d) is another important parameter revealing the distribution of the polarizing dust grains along a LOS (Bijas et al. 2022). It is known that the polarization measurement of a star can trace the polarizing dust grains present up to the distance of that star, assuming uniform B-field orientation all along the LOS. Observing a significant number of foreground stars, cluster members, and background stars towards a distant stellar cluster can trace the polarization properties of the dust present in the foreground, intracluster, and background mediums, respectively. If foreground dust contributes a non-negligible amount of polarization, then its removal from that of the cluster members is necessary to reveal the properties of intracluster dust. Likewise, if there exists a negligible amount of dust between a cluster and the background star, then the polarization of the latter can reveal the polarization properties of intracluster dust once the non-zero foreground contribution has

★ E-mail: bijasthejas@gmail.com (NB); eswaraiahc@labs.iisertirupati.ac.in (CE)
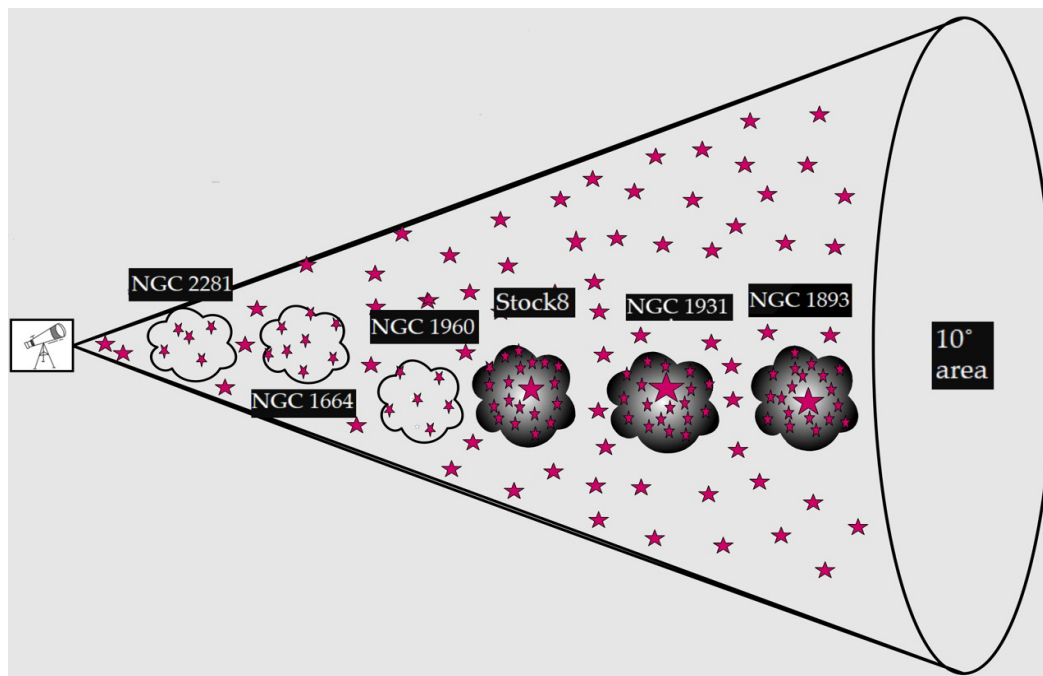
Figure 1. Schematic showing the stars located towards three older clusters NGC 2281, NGC 1664, and NGC 1960 (light grey) and three younger clusters Stock 8, NGC 1931, and NGC 1893 (dark), respectively. All six clusters are located at different distances but spread over a 10-deg area in the anticentre galaxy direction. The abundance of dust content is higher in younger clusters, while older clusters have a low dust content, as indicated by the dark and light grey colours of younger and older clusters. Note that the distances of clusters and the separation between them are not to scale.

Table 1. The basic parameters of all the six clusters distributed in the anticentre Galaxy direction. Note that the distances quoted in this table denote the overall distance to the stellar clusters identified from different publications.

Cluster-ID	Galactic longitude (l) (J2000; degree)	Galactic latitude (b) (J2000; degree)	Distance (kpc)	log (age) (Myr)
NGC 2281	174.90	+16.88	0.56	8.70
NGC 1664	161.68	−0.45	1.20	8.72
NGC 1960	174.54	+1.07	1.33	7.40
Stock 8	173.37	−0.18	2.05	6-6.70
NGC 1931	173.90	+0.28	2.30	6.0
NGC 1893	173.59	−1.68	3.25	6.60

Note. The quoted information for NGC 1931 has been taken from Pandey et al. (2013) and for the rest of the clusters is from Eswaraiah et al. (2011).

been taken care of. Therefore, by adding distance information to the polarization measurements, along with careful analyses, one can quantify the relative contribution of each component in comparison to the other towards a LOS. In addition, studying how the rate of polarization varies as a function of distance can help mark the distance boundary between foreground and intracluster dust. Such analyses can further help in revealing the polarization efficiency of foreground and intracluster dust. Previously, several studies have shown that the fraction of polarization (P) increases with distance (d) towards several targets, but confined to the solar neighbourhood (Eswaraiah et al. 2011; Wang et al. 2017; Lee et al. 2018) using polarization data from Heiles (2000) and distance data from Van Leeuwen (2007), respectively.

In the previous work, Bijas et al. (2022) have utilized A_V, distances, and polarization measurements of stars towards NGC 1893, and based on the analyses of P/A_V and P/d, they witness two dust populations. One exhibiting a higher polarization efficiency confined to $\lesssim 2$ kpc and another with a lower polarization efficiency to 2 kpc. However, in their work, they have combined field stars,

cluster members, and background stars to investigate overall trends based on P/A_V – A_V and P/d – d plots. Combining all the stars data towards one cluster would refrain from involving dust grains of several environments with different physical conditions. In this work, we test whether there exist two dust populations even after utilizing the data of six clusters located towards the anticentre Galaxy but distributed within a large area of $10°$ as shown in Fig. 1. Given the fact that these clusters lie at different evolutionary stages with varying stellar activity (see Table 1), dust in their intracluster mediums (ICM) may exhibit different polarization properties. In addition, since these clusters lie at different locations and distances within the Milky Way Galaxy, they may have different amounts of dust in their foregrounds and backgrounds, resulting in complex dust properties. Since all these clusters are located towards the anticentre Galaxy, by classifying the stars of each cluster into three groups such as foreground, background, and cluster members, and carefully testing the dust component that each group traces, we analyse P/A_V – A_V trends of the ISM and ICM dust. It is important to note that the polarization observations for the six clusters
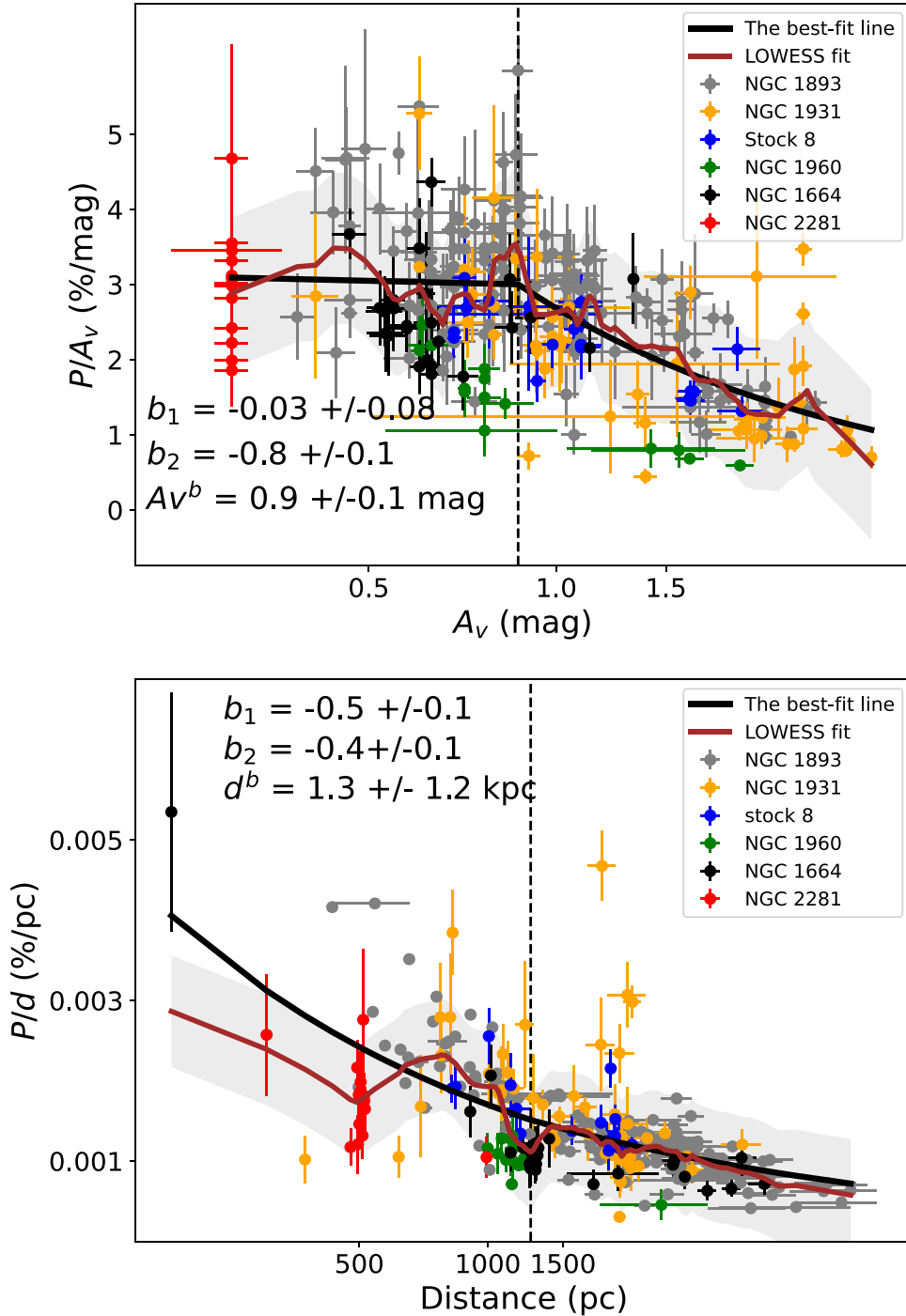
Figure 2. The overall P/A_V versus A_V plot (top) and P/d versus d plot (bottom). The best-fitting broken power law is denoted with a thick line. The dotted vertical line corresponds to A_V^b and d^b at which the power law breaks and the best-fitting parameters are overlaid. The overall trends traced by the LOWESS smoothed curves (brown) along with the corresponding 1-σ regions (grey) are also shown in both panels.

within the 10-deg area are obtained from slightly different lines of sight (LOSs), which cover a relatively small portion of the sky. Therefore, throughout this work, we assume that the light from all the clusters passes through a similar dust content of ISM and that the properties of the dust do not significantly vary from one LOS to another.

The structure of this paper is as follows. Section 2 describes various data sets, utilized in this study, such as optical polarization,

distance, and extinction for the six clusters. Section 3 presents the analyses for examining the presence of two dust populations towards these clusters. This is followed by the classification of stars towards each cluster into foreground, background, and cluster members using unsupervised machine learning algorithms GMM and DBSCAN. This classification helps delineate the observed polarization contributions from ISM and ICM dust. We further detail the results based on $P/A_V - A_V$ relations for the ISM and ICM on the

basis of power-law fits. The results are discussed in Section 4. Finally, Section 5 summarizes our results and presents our conclusions.

2 DATA

In this work, we use the available data on polarization, extinction, and distance. The *V*-band polarization data of 14 stars towards NGC 2281, 27 stars towards NGC 1664, 15 stars towards NGC 1960, 21 stars towards Stock 8, and 52 stars towards NGC 1931. But for NGC 1893, the *I*-band polarimetric observations of 152 stars are considered (Bijas et al. 2022) in this analysis. All the data were acquired with the ARIES Imaging Polarimeter (AIMPOL) (Rautela, Joshi & Pandey 2004) mounted on the Cassegrain focus of the 104-cm Sampurnanand telescope at ARIES, Nainital, India. The details on the polarimetric observations towards NGC 2281, NGC 1664, NGC 1960, and Stock 8 can be found in Eswaraiah et al. (2011), for NGC 1931 in Pandey et al. (2013), and for NGC 1893 in Bijas et al. (2022). All the clusters, except NGC 1893, have *V*-band polarization data. To make the polarization data from all clusters uniform, the *I*-band polarization data of NGC 1893 (Bijas et al. 2022) were converted to *V*-band using the Serkowski law (Serkowski, Mathewson & Ford 1975)

$$P_I = P_{max} \exp\left[-K \ln^2\left(\frac{\lambda_{max}}{\lambda_I}\right)\right], \tag{1}$$

where P_I is the percentage polarization in the *I* band ($\lambda_I = 0.88\,\mu m$), P_{max} is the peak polarization, and is assumed to occur in the *V*-band ($\lambda_{max} = 0.55 \pm 0.01\,\mu m$; Eswaraiah et al. 2011). The Serkowski parameter *K* is estimated using the relation $K = c_1\lambda_{max} + c_2$, where $c_1 = 1.66 \pm 0.09$ and $c_2 = 0.01 \pm 0.05$ are the constants for the visible to near-infrared ($0.35\,\mu m < \lambda < 2.2\,\mu m$) regime (Whittet 1992). The uncertainties in P_I are estimated by propagating the uncertainties in P_{max}, λ_{max}, and *K*. Here after, P_I is treated as *P*.

The corresponding stellar distances are obtained from Bailer-Jones et al. (2021). Bailer-Jones catalogue has geometric and photogeometric distances based on the stellar parallaxes of 1.47 billion stars published in *Gaia* Early Data Release 3 (*Gaia* EDR3). Since simulated data and external validations show that photogeometric distances are a better estimate for distant and faint stars (Bailer-Jones et al. 2021), we use photogeometric distances for our study. The details of how the geometric and photogeometric distances are estimated can be found in Bailer-Jones et al. (2021). We cross-match the coordinates of stars with polarization data towards all the six cluster regions with the Bailer-Jones catalogue within 2.7, 4.6, 1.5, 2.2, 0.7, and 0.5 arcsec, respectively, matching radii to find the photogeometric distances of all the stars towards NGC 2281, NGC 1664, NGC 1960, Stock 8, NGC 1931, and of 151 stars towards NGC 1893.

The total extinction in *V*-band, A_V, are extracted from the 3D dust reddening map published in Green et al. (2019) using DUSTMAPS module in PYTHON. They have used the stellar photometry from optical Pan-STARRS 1 and near-infrared 2MASS along with the *Gaia* EDR2 distances to infer the dust reddening values. The details of the dust reddening map and the methods and equations used for extracting A_V values used in this study are described in detail in Bijas et al. (2022). Out of the obtained reddening values for all the stars, some stars without reliable distance information in the 3D dust reddening map have been removed. This was based on whether the LOS fit of cumulative reddening versus distance has converged in a given LOS and also whether the distance at which the extinction values are returned is accurate. Hence, we obtain A_V values for 13 stars towards NGC 2281, 25 stars towards NGC 1664, 14

stars towards NGC 1960, 21 stars towards Stock 8, 51 stars towards NGC 1931, and 143 stars towards NGC 1893, respectively.

3 ANALYSES

3.1 Overall P/A_V versus A_V relation towards the six clusters

In this section, we analyse how P/A_V varies as a function of A_V and P/d varies as a function of *d* towards a larger sky area of $10°$ diameter consisting of all the six clusters in the anticentre galaxy direction. This would help in understanding the overall variations in polarization properties of dust that exist in the foreground, background, and intracluster mediums.

The relation $P/A_V - A_V$ towards the six clusters are fitted with a broken power law of the form using the *scipy − curvefit* module in PYTHON:

$$y = \begin{cases} a\left(\frac{x}{A_V^b}\right)^{b_1}, & \text{for } x \leq A_V^b \\ a\left(\frac{x}{A_V^b}\right)^{b_2}, & \text{for } x > A_V^b, \end{cases} \tag{2}$$

where *x* is A_V, A_V^b is the A_V at which the power-law breaks, and *a* is a coefficient. The b_1 and b_2 are power-law indices before and after A_V^b. Similarly, the data of $P/d - d$ are also fitted with the broken power law of the form similar to equation (2), where A_V and A_V^b are replaced with distance (*d*) and distance break d^b at which the power-law breaks, respectively. Fig. 2 shows the data and corresponding best fits for $P/A_V - A_V$ and $P/d - d$, respectively. The best-fitting parameters are given in Table 3.

To determine whether the broken power-law model of $P/A_V - A_V$ and $P/d - d$ is a better fit than a single power law, we perform a reduced χ^2 test. For $P/A_V - A_V$, the χ^2 values for the broken power law and single power-law models were 64.74 and 74.53, respectively. This indicates that the broken power-law model is better for $P/A_V - A_V$ due to its lower χ^2 value. For $P/d - d$, the χ^2 values for both the broken and single power-law models were 0.049, suggesting that both models fit equally well. However $P/d - d$ relation is very complex (as indicated by the LOWESS curve discussed later in this section) and has a significant amount of scatter caused due to the data points of NGC 1931 (yellow) located beyond 1.5 kpc. Therefore, we opted for the broken power-law model as it is more capable of capturing complex trends in the data and is sensitive to the outliers when compared to single power law.

Based on the broken power-law fitting on $P/A_V - A_V$, shown in Fig. 2 (top), we find that the polarization efficiency (P/A_V) remains constant up to a threshold extinction, A_V^b, of 0.9 ± 0.1 mag with a power-law index of -0.03 ± 0.08. For $A_V > 0.9$ mag the dust polarization efficiency decreases with a power-law index of -0.8 ± 0.1. Similarly, the broken power law over the data of $P/d - d$, shown in Fig. 2 (bottom), reveals a steeply decreasing trend by the rate of polarization up to a break distance, d^b, of 1.3 ± 1.2 kpc by following an index of -0.5 ± 0.1. Thereafter, the rate of polarization still decreases, but with a shallower power-law index of -0.4 ± 0.1. In both $P/A_V - A_V$ and $P/d - d$ plots, the NGC 1931 data points (yellow) lying beyond $A_V > 1$ mag and distance > 1.5 kpc is seen to exhibit significant scatter. We overlaid the location of these data points on the *R*-band image of the NGC 1931 cluster and found that these stars were located near the nebulous region of NGC 1931 (Pandey et al. 2013), where the O/B type stars are located. Differential reddening within the cluster and the polarization contribution from

Table 2. Sample data table containing the Source ID, cluster name, type of tracer (ISM or ICM), equatorial coordinates, distance (from *Gaia* EDR3), Stokes parameters, proper motions, polarization rate, extinction, polarization efficiency, Intrinsic extinction and intrinsic polarization efficiency, along with their errors. efficiencies (for the ICM tracers).

Source_ID	Cluster	Tracer	RA (J2000) (degree)	Dec (J2000) (degree)	Distance $\pm \sigma$ (kpc)	Q $\pm \sigma$ (per cent)	U $\pm \sigma$ (per cent)
1811173402856344704	NGC 1893	ICM	80.6653	33.3717	3.00 ± 0.16	1.29 ± 0.20	−2.04 ± 0.21
181173677734249600	NGC 1893	ICM	80.7238	33.3921	2.22 ± 0.10	2.19 ± 0.55	−1.09 ± 0.55
181173677734250240	NGC 1893	ICM	80.7190	33.3869	2.32 ± 0.12	2.30 ± 0.56	−1.41 ± 0.56
181173299780581120	NGC 1893	ICM	80.7176	33.3843	2.35 ± 0.15	2.32 ± 0.35	−1.73 ± 0.35
181173334136868224	NGC 1893	ISM	80.6886	33.3713	0.86 ± 0.01	1.63 ± 0.26	−0.34 ± 0.26
181173265420842880	NGC 1893	ISM	80.6992	33.3686	0.94 ± 0.02	1.85 ± 0.43	−0.33 ± 0.43
180986009142382720	NGC 1893	ICM	80.7413	33.3687	2.68 ± 0.78	2.31 ± 0.56	−2.18 ± 0.56
180985768624207744	NGC 1893	ICM	80.7717	33.3593	2.87 ± 0.16	1.69 ± 0.72	−1.90 ± 0.72
181178389317231616	NGC 1893	ICM	80.6221	33.5140	3.01 ± 0.21	1.29 ± 0.14	−2.99 ± 0.14
181175017764036352	NGC 1893	ISM	80.6993	33.4761	0.84 ± 0.01	1.85 ± 0.24	−1.07 ± 0.24

$\mu_{RA} \pm \sigma$ (mas yr^{-1})	$\mu_{\mathrm{Dec}} \pm \sigma$ (mas yr^{-1})	$P/d \pm \sigma$ (per cent/kpc)	$A_V \pm \sigma$ (mag)	$P/A_V \pm \sigma$ (per cent/mag)	$A_{\mathrm{Vint}} \pm \sigma$ (mag)	$P_{\mathrm{int}}/A_{\mathrm{Vint}} \pm \sigma$ (per cent/mag)	–
−0.43 ± 0.02	−1.53 ± 0.02	0.8 ± 0.1	1.67 ± 0.12	1.49 ± 0.16	1.35 ± 0.32	0.69 ± 1.92	–
−0.38 ± 0.02	−1.48 ± 0.02	1.1 ± 0.3	0.79 ± 0.02	3.19 ± 0.72	0.47 ± 0.29	1.04 ± 4.02	–
−0.29 ± 0.02	−1.42 ± 0.02	1.2 ± 0.2	0.79 ± 0.02	3.50 ± 0.73	0.47 ± 0.29	1.28 ± 4.03	–
−0.28 ± 0.03	−1.27 ± 0.03	1.2 ± 0.2	0.79 ± 0.02	3.75 ± 0.47	0.47 ± 0.29	1.65 ± 4.86	–
1.29 ± 0.02	−3.93 ± 0.03	1.9 ± 0.3	0.63 ± 0.10	2.72 ± 0.60	–	–	–
−0.97 ± 0.02	−8.04 ± 0.02	2.0 ± 0.5	0.63 ± 0.10	3.07 ± 0.85	–	–	–
−1.00 ± 0.24	−0.80 ± 0.25	1.2 ± 0.4	1.07 ± 0.09	3.06 ± 0.60	0.74 ± 0.31	1.50 ± 3.54	–
−0.52 ± 0.02	−2.10 ± 0.02	0.9 ± 0.3	1.24 ± 0.11	2.11 ± 0.63	0.92 ± 0.31	0.73 ± 3.14	–
−0.90 ± 0.02	−0.68 ± 0.02	1.1 ± 0.1	1.07 ± 0.09	3.14 ± 0.31	0.74 ± 0.31	2.44 ± 3.81	–
−3.15 ± 0.02	−0.81 ± 0.02	2.6 ± 0.3	0.68 ± 0.02	3.23 ± 0.37	–	–	–

the nebulous medium could be the reasons behind the observed scatter. Similarly, the NGC 2281 data points (red) are seen to exhibit scatter with $P/A_V > 1.5$ per cent mag in the $P/A_V - A_V$ plot [Fig. 2 (top)]. We assessed their impact on the fit by excluding them. Despite their removal, the consistency of the fit was maintained, indicating that these points have only a minimal impact on the fitting process.

From the overall trends in $P/A_V - A_V$ and $P/d - d$ relations, we see that they match with the results from previous work (Bijas et al. 2022) in which they observed similar trends in P/A_V and P/d towards the NGC 1893. This confirms the existence of two dust populations: foreground and Perseus dust, the former with higher polarization efficiency and a lower rate of polarization and the latter with lower polarization efficiency and a slightly higher rate of polarization, present in a 10-deg diameter in the anticentre galaxy direction as shown in Fig. 1.

Even though the results based on the power-law fits (Fig. 2) look similar to those seen towards NGC 1893 (Bijas et al. 2022), there is a difference in the overall data distribution in the plots of P/A_V versus A_V. In the case of NGC 1893, the data distribution is notably smooth as shown in the top panel of fig. 4 of Bijas et al. (2022). However, when all clusters are taken into account, there are several noticeable deviations from this smooth trend, as clear from LOWESS smoothed curves (brown) shown in Fig. 2. The curves are drawn using locally weighted scattered smoothing (LOWESS) algorithm (Cleveland 1979) with a frac parameter of 0.1, using *statsmodels* package in PYTHON. These variations are attributed to a well-mixed foreground/background and cluster member stars, which could trace dust polarization properties of interstellar and intracluster mediums, respectively. Moreover, the ISM dust properties towards one LOS may differ from other LOSs. Similarly, the dust properties in the ICM of one cluster might not be similar to that of another due to the difference in the amount of the intracluster medium, number of O/B type stars, etc. Therefore, it will be highly difficult to interpret the fluctuating trends in the P/A_V versus A_V plots of various clusters.

This is especially pronounced if clusters chosen have different ages, varying amounts of foreground/background, and intracluster mediums.

To facilitate a comprehensive understanding of the dust polarization efficiency of the dust in the ISM and ICM, one has to separate the total observed stars into foreground and background stars, and cluster members. Then, by using P and A_V of them, we will study the polarization efficiencies of dust in the ISM and ICM.

3.2 Identification of stars tracing ISM and ICM dust

To separate the observed polarization contributions towards six clusters into the ISM and ICM components, it is essential to classify all the stars with polarization and distance data into foreground, cluster, and background stars. Since the member stars of a cluster are believed to be formed by the same parental cloud, they are expected to be located at the same distances. In addition, their light will pass through similar amounts of foreground column density resulting in similar amounts of fraction of polarization (based on the average relation between polarization and extinction ($P = 5 E(B − V)$ or $P = 1.6 A_V$; assuming $R_V = 3.1$; Serkowski et al. 1975). Therefore, in the polarization versus distance plot, cluster members are expected to exhibit a conspicuous grouping or clustering. In contrast, both foreground (which lie between the cluster and the observer) and background (lie behind the stellar cluster) stars show a scattered distribution depending upon their distances and the amount of extinction they encounter.

In addition, considering the proper motion of stars provides another crucial parameter for classifying stars into field and cluster members. This is due to the fact that all stars within a cluster being part of a gravitationally bound system can exhibit similar, albeit smaller, proper motions in comparison to the foreground field stars resulting in a clustered distribution in the proper motion plot (μ_{RA} versus μ_{Dec}; example see top panel of fig. 8 of Bijas et al. 2022).
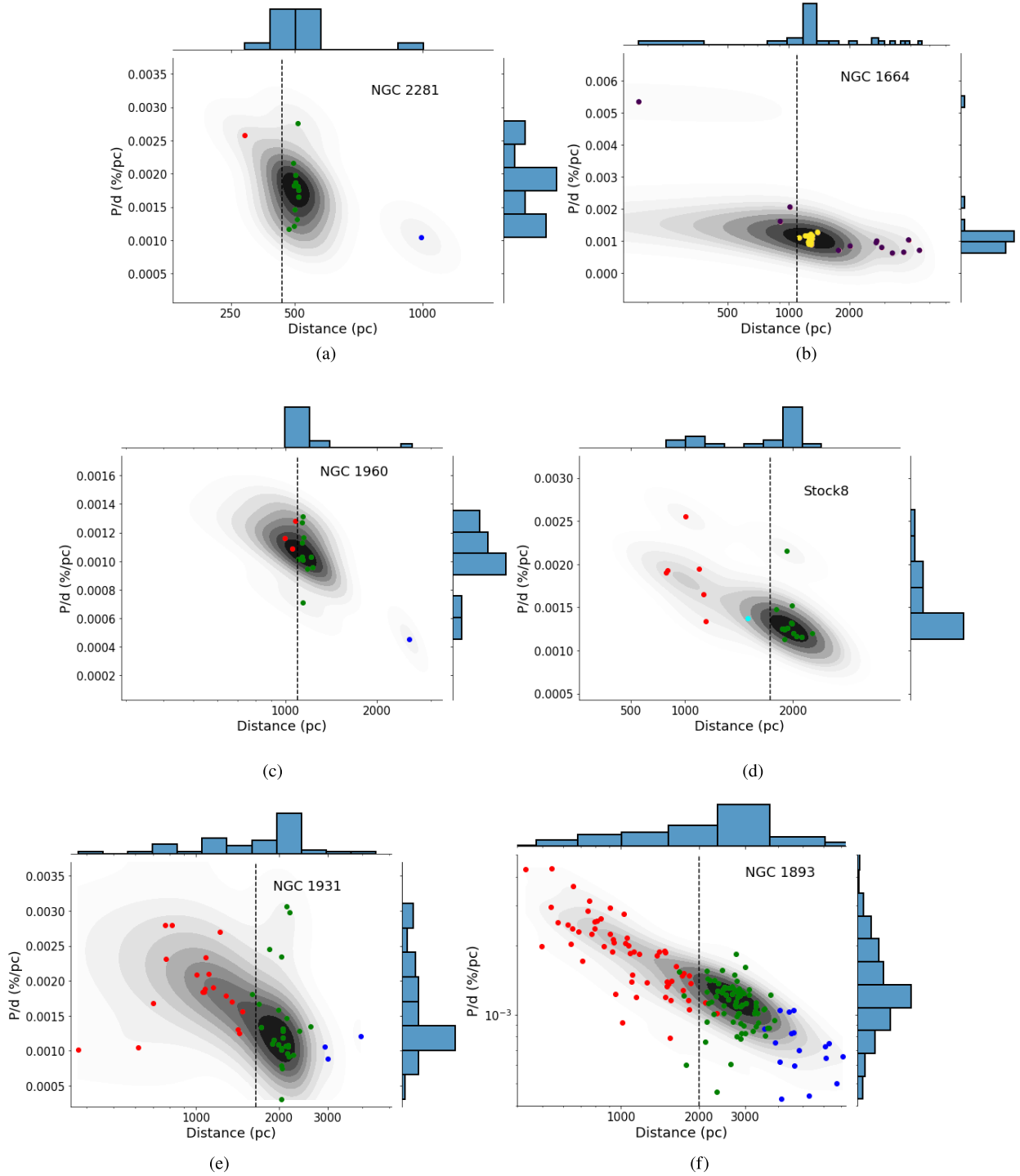
Figure 3. The *P/d* versus distance (*d*) relations towards each cluster. In panels (a), (c), (d), (e), and (f), three groups of stars-foreground stars , cluster members, and background stars, identified by the GMM, are overlaid. Note that Stock 8 (panel d) does not have background stars and has two groups of foreground stars identified by the GMM instead. Panel (b) shows the two groups of stars, foreground stars and cluster members, identified by DBSCAN. The darker background in all panels corresponds to the higher probability density, whereas the lighter density for the lower probability density. The vertical dotted lines in each figure denote the transition distance, where the transition from ISM to ICM is observed. 1D histograms in each panel are also shown.

In contrast, foreground stars, being closer than the cluster members and not part of a gravitationally bound system, will exhibit higher proper motions. Background stars, located farther than the cluster members, will display proper motions similar to those of the cluster members (see fig. 9 of Bijas et al. 2022). Therefore, combining the

distance information of the stars with the polarization data and proper motions offers a 3D perspective on the location of each star towards a particular LOS, yielding reliable membership information.

To separate the observed stars into cluster and field stars, we employ two unsupervised *clustering* algorithms such as the Gaus-

Table 3. Best-fitting parameters, based on the broken power law of overall $P/A_V - A_V$ and $P/d - d$ towards all the clusters, single power law of $P/A_V - A_V$ towards the ISM, and single power law of $P_{int}/A_{Vint} - A_{Vint}$ towards the ICM, respectively.

Cluster-ID	Relation	a	b	b_1	b_2	A_V^b or d^b
Overall relations	$P/A_V - A_V$	3.0 ± 0.1	–	-0.03 ± 0.08	-0.8 ± 0.1	0.9 ± 0.1 mag
	$P/d - d$	0.0015 ± 0.0007	–	-0.5 ± 0.1	-0.4 ± 0.1	1.3 ± 1.2 kpc
ISM	$P/A_V - A_V$	2.3 ± 0.1	-0.3 ± 0.1	–	–	–
ICM	$P_{int}/A_{Vint} - A_{Vint}$	1.4 ± 0.1	-0.7 ± 0.1	–	–	–
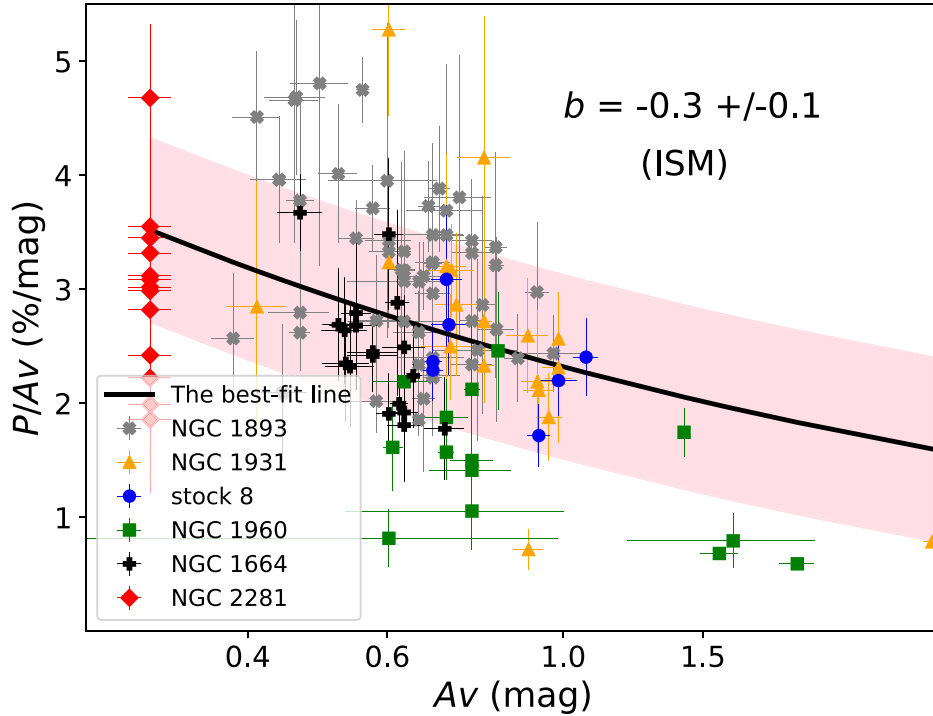
Figure 4. P/A_V versus A_V plot in the ISM. The best-fitting power law is denoted with a thick line, and the corresponding 1-σ confidence region is shown as a shaded area. The best-fitting power-law index is also overlaid.

sian Mixture model (GMM) for NGC 2281, NGC 1960, Stock 8, NGC 1931, and NGC 1893 and the Density-Based Spatial Clustering of Applications with Noise (DBSCAN) for only one cluster NGC 1664. The choice of the above-mentioned unsupervised algorithms for classifying purposes depends mostly on the parameters such as the number of mixture components ($n_{components}$) for GMM, epsilon (ϵ) and minimum number of points (*MinPts*) for DBSCAN as well as the probability density structure of each data set. While in the case of the five clusters, we found the GMM-predicted clusters could trace the background density structure, in the case of NGC 1664 it failed to do so. Therefore, for NGC 1664 we decided to go with DBSCAN, the next-best algorithm that can predict clusters based on their density.

The GMM analyses are applied on the $P/d - d$ plots, by providing, distance *d*, Stokes parameters *Q* and *U*, proper motions μ_{RA} and μ_{Dec} (obtained from *Gaia* EDR3 catalogue) and their corresponding errors as input using the *scikit − learn* module in PYTHON. A sample data table consisting of the input parameters, P/d, and P/A_V are given in Table 2. The GMM is based on the assumption that data instances come from multiple Gaussian distributions with unknown mean and covariance values (Melchior & Goulding 2018; Cantat-Gaudin et al. 2019). It is a useful algorithm for grouping stars according to their properties. GMM assigns a probability for

each star to be part of a particular group using an Expectation-Maximization (EM) algorithm. The EM algorithm starts off by assigning group parameters to the stars and then iteratively performs two steps – expectation and maximization, until it converges. In the expectation step, the EM algorithm calculates the probability for each star belonging to a particular group based on the current group parameters. In the maximization step, the EM algorithm updates each group based on all the stars in the group, with each star weighed by the probability that it belongs to that group. We give two parameters as input to GMM for performing the classification: (i) $n_{components} = 3$ as we expect three groups of stars along a LOS and (ii) random state $= 0$ or 1 for maintaining consistency in the classification. The GMM has categorized the total sample of stars towards each stellar cluster into the foreground (red and cyan), cluster members (green), and background stars (blue), which are shown in Figs 3(a), (c), (d), (e), and (f). The information on probability density and frequency distributions are also shown in the figures with black/grey background and histograms, respectively.

Similarly, DBSCAN classifies cluster members and field stars towards NGC 1664 using the *scikit − learn* package. DBSCAN identifies clusters by grouping data points together in dense regions and identifies data points in low-density regions as noise or outliers (Ester et al. 1996; Schubert et al. 2017). It uses two input param-
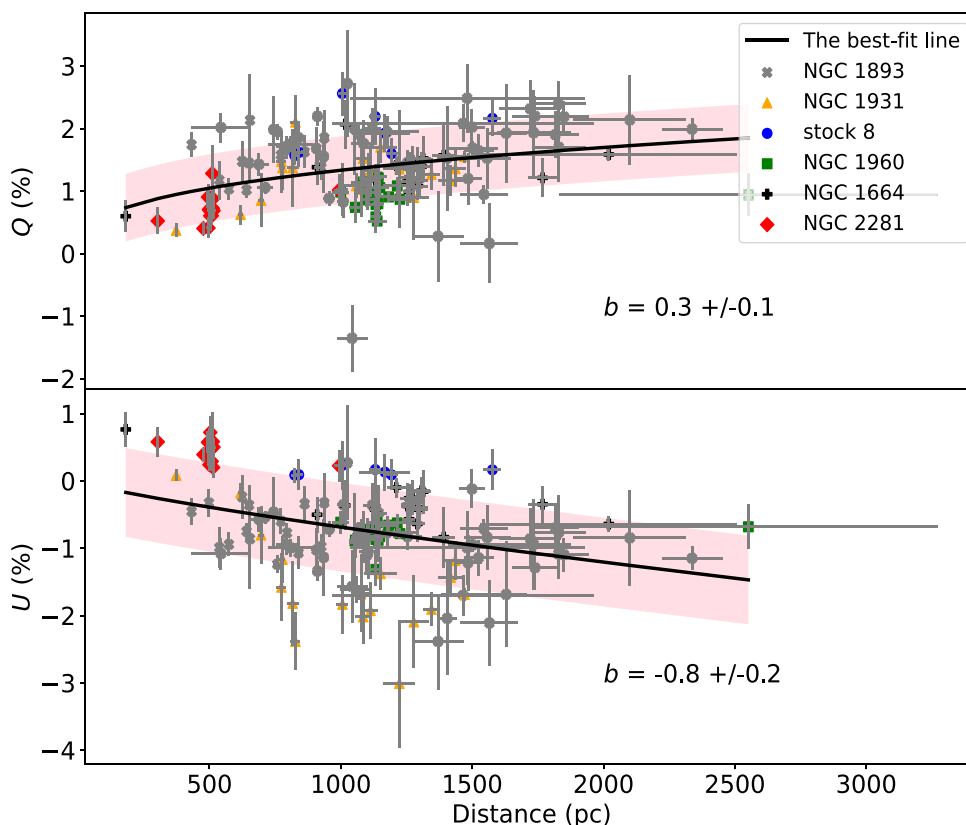
Figure 5. Q (top) and U (bottom) versus distance plots of the ISM tracers (foreground stars of both young and old clusters as well as cluster members of old clusters). In both plots, Stokes parameters of six stars belonging to NGC 1664 have been removed because they fell off from the main distribution and did not affect the overall fit. The power-law fit is denoted with a thick line. The best-fitting parameters are also overlaid. The corresponding 1-σ confidence regions are shown as shaded areas in both panels. The corresponding transition distance identified by the GMM is denoted by the vertical black dotted line.

Table 4. The foreground polarization and extinction values of the three young clusters in the anticentre Galaxy direction.

Cluster-ID	Q_{fg} (per cent)	U_{fg} (per cent)	A_{Vfg} (mag)
Stock 8	1.66	−1.12	0.41
NGC 1931	1.62	−1.05	0.34
NGC 1893	1.73	−1.23	0.33

eters, epsilon (ϵ) and the minimum number of points (*MinPts*), to determine the density of the clusters. To start clustering, the algorithm randomly selects a point and searches for neighbouring points within a radius of ϵ. If the number of neighbouring points is greater than or equal to *MinPts*, a cluster is formed, and the algorithm expands the cluster by adding all the points within the ϵ distance of the initial cluster. The algorithm then identifies the next unassigned point and repeats the process until all points are assigned to a cluster. It is important to note that the parameters for DBSCAN are specific to the distribution of individual data sets. In the case of the NGC 1664 cluster, ϵ, and *Minpts* parameters were fixed at 90 and 5, respectively. The DBSCAN-identified field (violet) and cluster members (yellow) towards NGC 1664, along with the probability density and frequency distributions are shown in Fig. 3(b).

The distance at which the transition from the foreground medium to the intracluster medium occurs can be determined by the fact that the number of stars and, hence, the background density in-

crease abruptly, and thereafter, a cluster of data points appears as shown in Figs 3(a)–(f). The clusters NGC 1893, NGC 1931, Stock 8, NGC 1960, NGC 1664, and NGC 2281 exhibit transition distances (note that the *distance break* based on the power-law break shown in Fig. 2 is different from the transition distance) of 2, 1.65, 1.79, 1.1, 1.2, and 0.45 kpc, respectively, as denoted with vertical dotted lines in Figs 3(a)–(f).

Three of the six clusters, Stock 8, NGC 1931, and NGC 1893, we analyse are young, and the other three, NGC 2281, NGC 1664, and NGC 1960 are old (see Table 1). Since younger clusters contain leftover cloud material, the background stars may show polarization properties similar to those of cluster members. So we consider stars lying beyond the transition distance to be cluster members and background stars representing ICM dust, and stars up to the transition distance to be foreground stars revealing ISM dust. However, the old clusters are supposed to have a negligible dust content; hence, the excess amount of polarization from the old cluster member's ICM should be near zero. As a result, the cluster members, background stars, and foreground stars along the LOSs of old clusters can trace the ISM very well. Consequently, it is reasonable to assume we can only trace the polarization properties of ICM dust in younger clusters and not in older clusters.

We have adopted the following assumptions for characterizing the polarization properties of ISM and ICM dust: (a) ISM dust is traced by foreground stars of all young and old clusters, plus cluster members and background stars of old clusters (hereafter
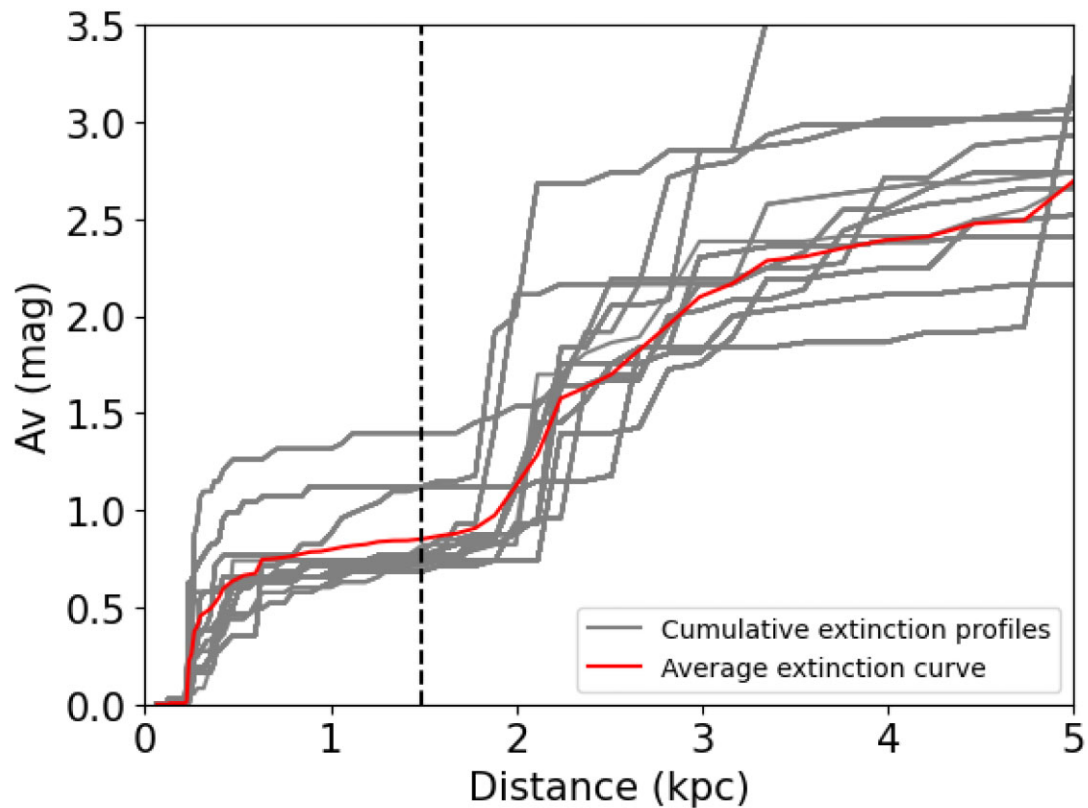
Figure 6. Cumulative A_V versus distance profiles along all lines of sights in the 4.6 arcmin radius area around Stock 8. The average extinction profile is also shown.
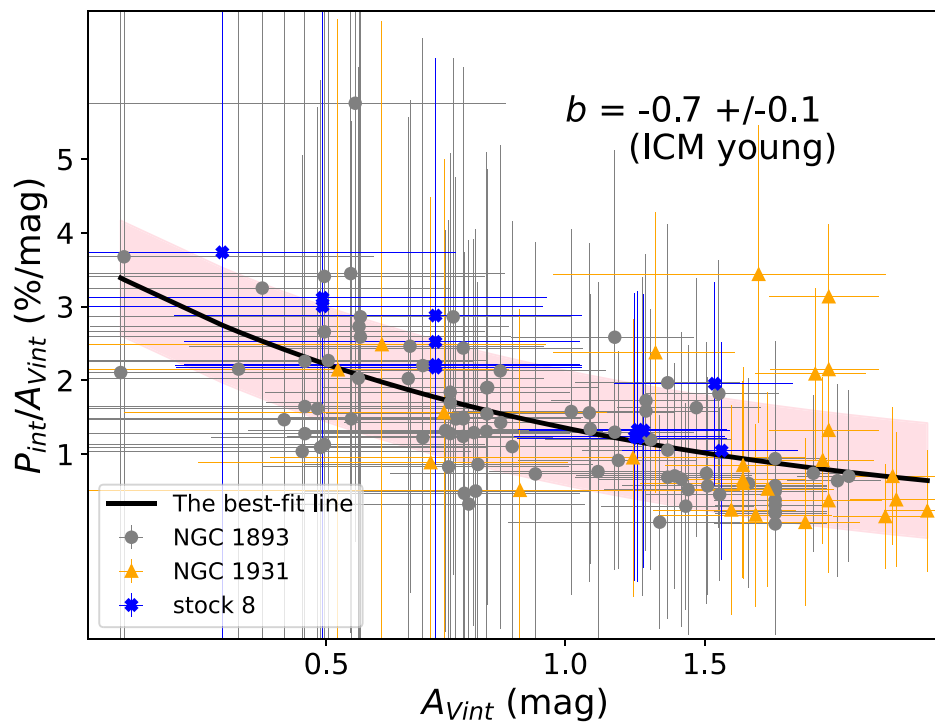

Figure 7. P_{int}/A_{Vint} versus A_{Vint} plot in the ICM. The best-fitting power law is denoted with the thick line, and the corresponding 1-σ confidence region is shown as a shaded area. The best-fitting power-law index is also overlaid.
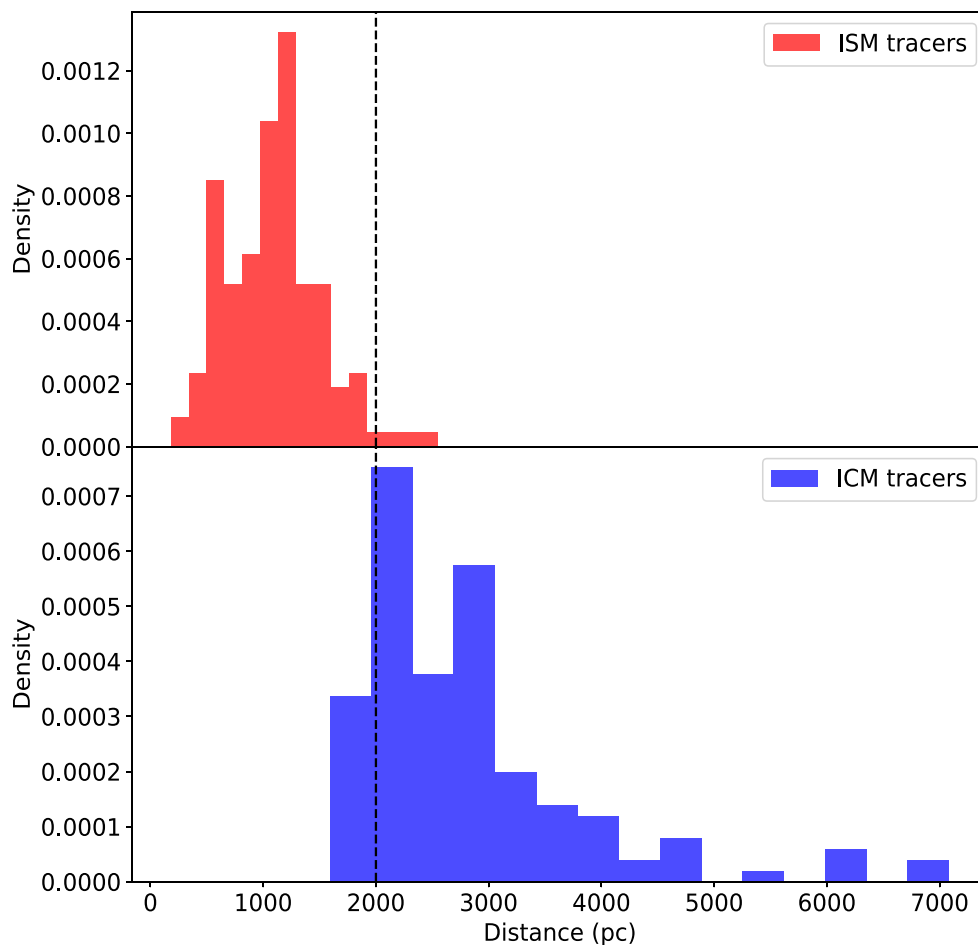
Figure 8. Histograms of the stars tracing the ISM dust (top) and ICM dust (bottom). The dotted vertical lines in both figures denote the transition distance of 2 kpc.

ISM tracers); (b) ICM dust is traced by both cluster members and background stars of young clusters (hereafter ICM tracers). By extracting P, A_V, and distance values of all the ISM and ICM tracers, we analyse $P/A_V - A_V$ relations separately for the dust in ISM and ICM.

3.3 P/A_V versus A_V of ISM tracers

The relation $P/A_V - A_V$ of the ISM dust towards the six clusters are fitted with a single power law of the form $y = a(x)^b$ using *scipy − curvefit* module in PYTHON, where x is A_V, a is a coefficient, and b is the power-law index. The best-fitting parameters and the plot for $P/A_V - A_V$ relation towards ISM of the six stellar clusters are given in Table 3 and Fig. 4, respectively. Based on the single power-law fit over $P/A_V - A_V$ data of ISM, we infer that the P/A_V declines with A_V with an index of -0.3 ± 0.1. A sample data table containing the extinction (A_V) and polarization efficiencies (P/A_V) of the ISM tracers is given in Table 2.

3.4 Intrinsic P and A_V of ICM tracers

The polarization and extinction values of ICM tracers (cluster members and background stars) cannot be used directly to infer the properties of ICM dust. This is because they still contain the contribution from foreground dust; therefore, it is essential to

quantify and subtract the same to shed light on the ICM dust. To do this, we extract the Stokes parameters Q and U of ISM tracers using the relations $Q = P\cos(2PA)$ and $U = P\sin(2PA)$, where P and PA are the fraction of polarization and position angle of B-field inferred by ISM tracers.

Further, we perform power-law fits (similar to as described in Section 3.3) on the Stokes parameters versus distance plots shown in Fig. 5 by considering the data of ISM tracers. From the solution, we then estimate the resultant Stokes parameters at the transition distance for each young cluster identified from GMM or DBSCAN, which are treated as foreground Stokes parameters, Q_{fg} and U_{fg}, and are listed in Table 4. These are vectorially subtracted from the Stokes parameters of ICM tracers to obtain the intrinsic Stokes parameters for each young cluster using the following relations

$$Q_{int} = Q - Q_{fg}$$
$$\text{and } U_{int} = U - U_{fg}. \tag{3}$$

Finally, the intrinsic fraction of polarization corresponding to ICM dust is derived using

$$P_{int} = \sqrt{Q_{int}^2 + U_{int}^2}. \tag{4}$$

Similarly, to determine foreground extinction towards three clusters Stock 8, NGC 1931, and NGC 1893, we extract distance versus
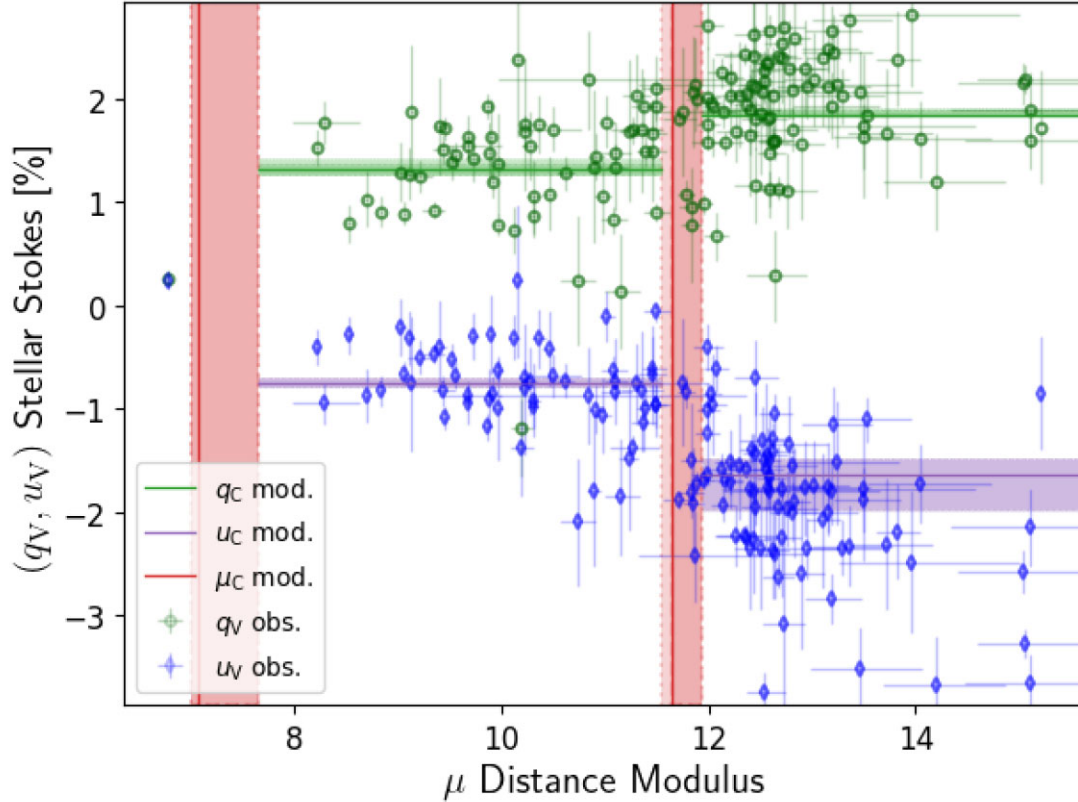
Figure 9. The stellar Stokes parameters q_V (circles) and u_V (diamonds) versus distance modulus (μ) plot from BISP-1 two dust layer model. The horizontal lines denote the posterior mean Stokes parameters q_C mod. and u_C mod. of each cloud, respectively. The vertical lines denote the mean distance moduli corresponding to the mean posterior parallaxes of the two clouds. In each case, the corresponding shaded regions indicate the 95 percentile (light shade) and 68 percentile (dark shade) confidence regions.

cumulative extinction, A_V, profiles within a circular radius of 4.6, 7.1, and 10.5 arcmin area, respectively, around each cluster. For this, we make use of the 3D extinction map of Green et al. (2019) and DUSTMAPS module in PYTHON. Fig. 6 depicts the distance versus extinction profiles for Stock 8. We take the average extinction from multiple extinction values at each distance and plot the average extinction profile (red curve) in Fig. 6. The mean A_V at the transition distance is considered the foreground extinction A_{Vfg} towards each cluster and is listed in Table 4. We then subtract this A_{Vfg} from the A_V values of the ICM tracers by utilizing the relation $A_{Vint} = A_V - A_{Vfg}$.

3.5 P_{int}/A_{Vint} versus A_{Vint} relations towards the ICM

To examine the trends in the dust polarization efficiency in the ICM using the foreground subtracted P_{int} and A_{Vint} (cf. Section 3.4), the $P_{int}/A_{Vint} - A_{Vint}$ relations towards the three younger clusters Stock 8, NGC 1931, and NGC 1893 are plotted and are fitted with a power law. The $P_{int}/A_{Vint} - A_{Vint}$ plots with the corresponding fit for the ICM are shown in Fig. 7. From the figure, we see that the P_{int}/A_{Vint} in the ICM decreases with a power-law index of -0.7 ± 0.1. The best-fitting parameters are given in Table 3. A sample data table containing the intrinsic extinction (A_{Vint}) and intrinsic polarization efficiencies (P_{int}/A_{Vint}) of the ICM tracers is given in Table 2.

4 DISCUSSION

The power-law fits on $P/A_V - A_V$ and $P_{int}/A_{Vint} - A_{Vint}$ of ISM and ICM tracers suggest different power-law indices of -0.3 and -0.7, respectively. These indices imply efficient dust grain alignment in the general diffuse ISM than those dust grains in the ICM. This is further evidenced by the fact that, despite having a smaller mean A_V of 0.7 ± 0.3 mag, the ISM exhibits relatively a higher mean P/A_V of 2.7 ± 0.9 per cent mag^{-1}. In contrast, the ICM with a higher mean A_{Vint} of 1.1 ± 0.6 mag shows a smaller P_{int}/A_{Vint} of 1.5 ± 1.0 per cent mag^{-1}. Even though different mechanisms have been proposed to explain how the dust grains are getting aligned with the magnetic fields to produce higher polarization, the most established has been the radiative torque (RAT) alignment mechanism (Dolginov & Mytrophanov 1976; Draine & Weingartner 1996; Lazarian & Hoang 2007). According to the RAT mechanism, when a radiation field is incident upon the dust grains, it spins the dust grains to higher angular momentum and hence can efficiently align them with the local magnetic fields. These efficiently aligned dust grains then cause a higher level of polarization. Therefore, higher radiation field strength can result in better dust grain alignment and increased polarization. Similarly, the size of the dust grains is another important factor determining the extent of dust alignment. If the dust grains are too large, RATs will become inefficient in rotating them. On the other hand, if the dust grains are too small, they may be spherical to scatter radiation anisotropically and generate RATs. As
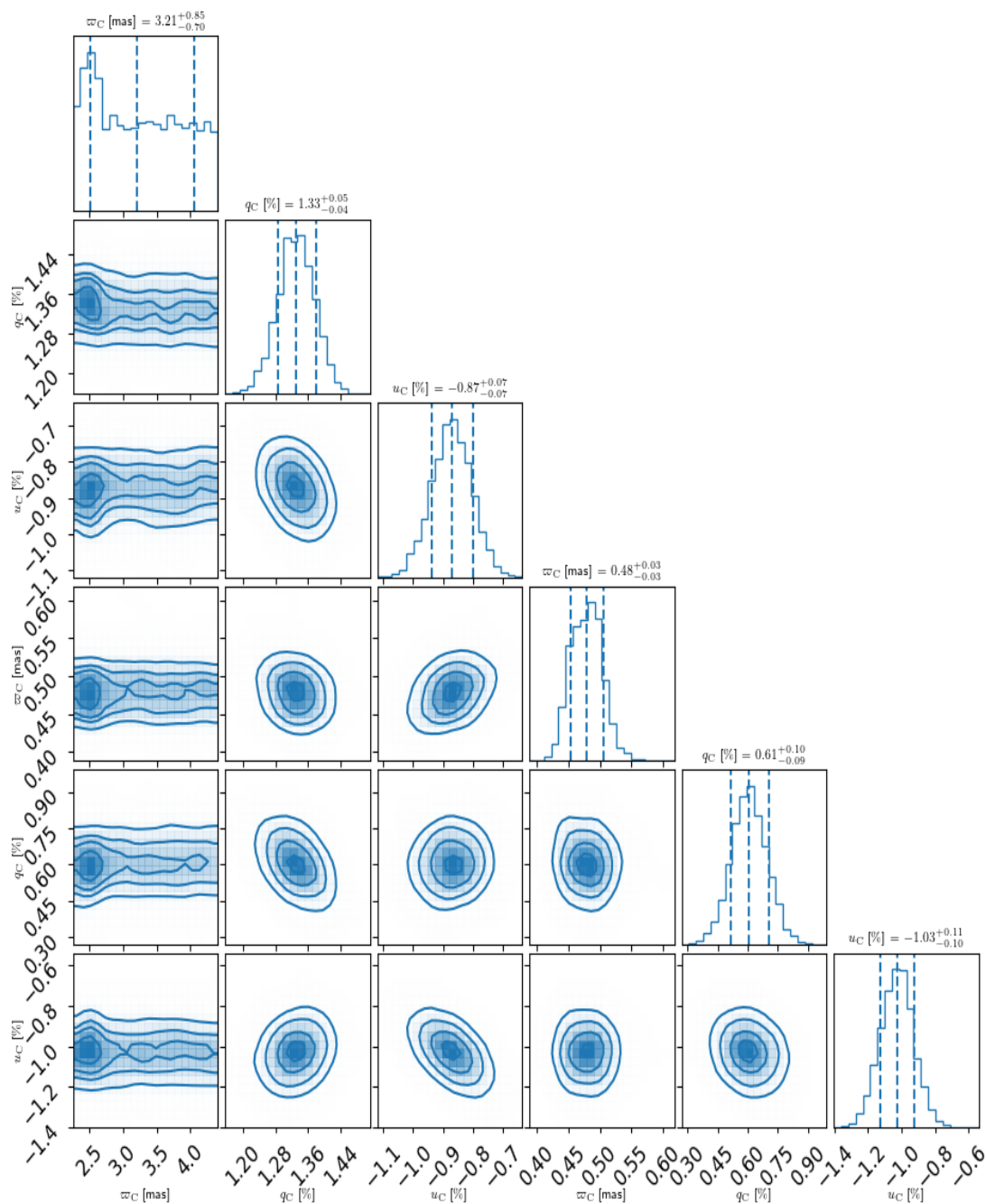
Figure 10. The posterior distributions of the cloud parallaxes (ϖ_C, in units of milliarcseconds) and mean Stokes parameters (q_C and u_C, in units of per cent) for the two dust layer model produced by BISP-1. The vertical dashed lines indicate 16, 50, and 84 percentiles of each posterior distribution. The values at the top of each panel contain the mean, minimum, and maximum values of each parameter corresponding to the 68 per cent confidence interval.

a result, only larger submicron-sized dust grains that are neither too big nor too small tend to align well with magnetic fields (Whittet 2004).

The diffuse ISM receives a higher amount of interstellar radiation field, which can result in stronger RATs that rotate the dust grains to higher angular momentum, leading to better alignment with the local magnetic field and producing a higher fraction of interstellar polarization as seen in Fig. 4. To explain the poor alignment of dust grains observed in the ICM compared to ISM, it is essential to

probe the intracluster medium conditions of the three young clusters: Stock 8, NGC 1931, and NGC 1893.

Out of the three clusters, NGC 1893 is the youngest followed by Stock 8 and NGC 1931, respectively, with NGC 1893 having the highest number of O/B type stars followed by Stock 8 and NGC 1931 (Bonatto & Bica 2009; Damian et al. 2021; Quintana, Wright & Jeffries 2023). As shown in Fig. 7, NGC 1893 exhibits relatively higher polarization efficiency (P_{int}/A_{Vint}) among the three clusters, followed by Stock 8 and NGC 1931. This difference in polarization

efficiencies can be attributed to the varying number of O/B type stars, as a higher number of such stars can produce more energetic UV radiation, leading to stronger RATs that efficiently align the dust grains and produce higher polarization in NGC 1893 as compared to the other two clusters. Similarly, NGC 1931 contains relatively bigger-sized dust grains as inferred by the abnormal reddening law observed in the ICM of NGC 1931 with a R_V value of 5.2 ± 0.3 (Lim et al. 2015). In addition, Jose et al. (2008) has found the presence of small-sized dust grains and small polycyclic aromatic dust grains in the intracluster medium of Stock 8 using the MIR emission based on Midcourse Space Experiment (MSX).

The conditions in the ICM of younger clusters, as described above, can have several consequences for the alignment of dust grains with magnetic fields and the resulting polarization efficiencies. For instance, all three young clusters, especially NGC 1893 have strong radiation feedback and ionization shocks emanating from the massive O/B type stars which heat the gas in the ICM (Jose et al. 2008; Pandey et al. 2013; Lim et al. 2018; Damian et al. 2021). This increased gas temperature in the ICM of the younger clusters may be causing increased gas-dust collisions, which might be misaligning the dust grains in the ICM. Similarly, due to bigger and smaller sized dust grains in the ICM of NGC 1931 and Stock 8, respectively, RATs can become ineffective in aligning the dust grains with the magnetic field. Hence, a combined effect of all these possible scenarios in action can explain the overall lower polarization efficiency of dust grains seen in the ICM vis-à-vis ISM. This demonstrates that our polarization data can trace the POS magnetic fields and dust properties of ISM dust very well owing to efficient dust grain alignment, but does poorly in the ICM dust of young clusters due to relatively inefficient dust grain alignment.

As per the distribution of distances shown in Fig. 8, it is evident that the ISM tracers are confined up to 2 kpc, whereas the ICM tracers lie beyond 2 kpc. We have witnessed this distance boundary of 2 kpc where ISM and Perseus dust have been apportioned towards the direction of NGC 1893 (Bijas et al. 2022). Therefore, the current study based on the data of several clusters confirms that there exist two dust populations that are separated at 2 kpc. It is worth noting here that the proposed Perseus dust by Bijas et al. (2022) and the termed ICM dust in this work should be the same because the stars lying beyond 2 kpc must either be part of young clusters or background stars tracing ICM dust.

To confirm the 2 kpc boundary between two dust components of ISM and ICM, and to quantify the relative polarization contribution of each component independently, we used the recently published PYTHON package BISP-1[1] (Pelgrims et al. 2023). BISP-1 uses an LOS inversion method to decompose the observed polarization into individual polarization contributions from each dust cloud along the LOS. We gave the observed Stokes parameters (q_V, u_V), parallaxes, and their corresponding errors of all the stars towards the six clusters as input to the BISP-1 package. A two-dust layer model was invoked to predict the posterior mean Stokes parameters (q_C mod. and u_C mod.) and distance moduli (μ_C mod.) of the individual dust clouds contributing to the overall polarization. The two-dust layer model consisted of 12 flat prior distributions (2 for each parameter corresponding to the minimum and maximum values), and a dynesty sampler was used to sample the parameter space to produce the posterior distributions using 50 000 sampling points. Details on how the two-dust layer model was chosen as the best model are given in Appendix A. The resulting Stokes parameters versus distance

modulus plot are shown in Fig. 9, and the corresponding posterior distributions of each cloud's parallaxes and Stokes parameters are given in Fig. 10. From both figures, we see that BISP-1 predicts two dust layers: (i) the first dust layer tracing the foreground medium starts at a distance of $\sim$0.31 kpc ($\mu = 7.44$) and (ii) ICM dust appearing from 2.1 kpc onwards ($\mu = 11.5$) traces the intracluster medium. Using the mean posterior values of the Stokes parameters of the individual clouds (q_C and u_C), we estimated the percentage polarization for each. It was seen that the ISM dust cloud has a higher percentage of polarization of 2.3 per cent and is a major contributor to the overall polarization than the ICM dust cloud, with a polarization of 1.5 per cent. Note that the BISP-1-yielded ICM contribution takes care of the foreground contribution. Therefore, ISM dust contributes a higher amount of polarization than that of ICM.

We also estimated the mean polarization angles of the two dust clouds using the Stokes parameters, which were found to be 163.4° and 150.1°, respectively. The similar polarization angles of the ISM and ICM dust clouds indicate that the B-field in the ISM and ICM is nearly the same. This means that the changes observed in the polarization efficiencies in the ISM and ICM are not due to a change in the orientation of B-fields along the LOS of target clusters, but due to differences in the properties of ISM and ICM dust. This result, therefore, also supports results of Bijas et al. (2022), which have also reported higher alignment efficiency of foreground dust up to 2 kpc and poor alignment efficiency of Perseus dust after 2 kpc despite having uniform B-field orientation towards NGC 1893.

5 SUMMARY AND CONCLUSIONS

Our study aims to understand the changes in dust polarization efficiencies in the ISM and ICM using the polarization data of three older and three younger clusters. These clusters are spread over a 10-deg large area towards the anticentre galaxy. To achieve this, we categorize the stars of each cluster into those tracing ISM and ICM dust using two clustering algorithms GMM and DBSCAN. We then analysed the variations in the polarization efficiency as a function of extinction in (i) diffuse ISM, and (ii) ICM of younger clusters by utilizing *V*-band polarization data from the ARIES IMaging POLarimeter (AIMPOL) (Eswaraiah et al. 2011; Pandey et al. 2013; Bijas et al. 2022), distances from Bailer-Jones et al. (2021), and extinction data from Green et al. (2019). Our findings suggest more efficiently aligned dust grains in the ISM than those in the ICM of younger clusters, possibly due to the unfavourable dust sizes and physical conditions in the ICM. We also found that ISM and ICM dust are separated at 2 kpc distance which is in accordance with our previous findings (Bijas et al. 2022). Further, we have used the LOS inversion technique, BISP-1 (Pelgrims et al. 2023) to confirm the distance boundary of 2 kpc and to quantify the relative polarization contribution of ISM and ICM dust. BISP-1 shows that ISM dust contributes a higher amount of fraction of polarization in comparison to ICM dust. BISP-1 also reveals that the mean B-field orientation in the ISM and ICM is nearly identical.

---

[1] https://github.com/vpelgrims/Bisp_1/

DATA AVAILABILITY

Partial data are given in Table 2. The complete data set can be accessed online from the Harvard Dataverse using the following link: https://dataverse.harvard.edu/dataset.xhtml?persistentId=doi%3A10.7910%2FDVN%2FHHYYGK&version = DRAFT

REFERENCES

Alves F. O., Frau P., Girart J. M., Franco G. A. P., Santos F. P., Wiesemeyer H., 2014, A&A, 569, L1

Bailer-Jones C. A. L., Rybizki J., Fouesneau M., Demleitner M., Andrae R., 2021, AJ, 161, 147

Bijas N., Eswaraiah C., Wang J.-W., Jose J., Chen W.-P., Li D., Lai S.-P., Ojha D. K., 2022, MNRAS, 515, 3352

Bonatto C., Bica E., 2009, MNRAS, 397, 1915

Cantat-Gaudin T. et al., 2019, A&A, 624, A126

Cashman L. R., Clemens D., 2014, ApJ, 793, 126

Chapman N. L., Goldsmith P. F., Pineda J. L., Clemens D., Li D., Krčo M., 2011, ApJ, 741, 21

Cleveland W. S., 1979, J. Am. Stat. Assoc., 74, 829

Damian B., Jose J., Samal M. R., Moraux E., Das S. R., Patra S., 2021, MNRAS, 504, 2557

Davis Leverett J., Greenstein J. L., 1951, ApJ, 114, 206

Dolginov A., Mytrophanov I., 1976, Astrophys. Space Sci., 43, 291

Draine B., Weingartner J. C., 1996, A&J, 470, 551

Ester M., Kriegel H.-P., Sander J., Xu X., Simoudis E., Han J., Fayyad U., 1996, A density-based algorithm for discovering clusters in large spatialdatabases with noise. Vol. 96, In knowledge discovery and data mining (kdd)p.226

Eswaraiah C., Pandey A., Maheswar G., Medhi B. J., Pandey J., Ojha D., Chen W., 2011, MNRAS, 411, 1418

Gerakines P., Whittet D., Lazarian A., 1995, ApJ, 455, L171

Goodman A. A., Jones T. J., Lada E. A., Myers P. C., 1992, ApJ, 399, 108

Goodman A. A., Jones T. J., Lada E. A., Myers P. C., 1995, ApJ, 448, 748

Green G. M., Schlafly E., Zucker C., Speagle J. S., Finkbeiner D., 2019, ApJ, 887, 93

Heiles C., 2000, AJ, 119, 923

Hiltner W., 1949, Science, 109, 165

Jones T. J., Bagley M., Krejny M., Andersson B.-G., Bastien P., 2014, AJ, 149, 31

Jose J. et al., 2008, MNRAS, 384, 1675

Lazarian A., Hoang T., 2007, MNRAS, 378, 910

Lee C., Eswaraiah C., Chen W.-P., Pandey A., 2018, AJ, 156, 115

Lim B., Sung H., Bessell M. S., Kim J. S., Hur H., Park B.-G., 2015, AJ, 149, 127

Lim B. et al., 2018, MNRAS, 477, 1993

Melchior P., Goulding A. D., 2018, Astron. comput., 25, 183

Pandey A. K. et al., 2013, ApJ, 764, 172

Pattle K. et al., 2019, ApJ, 880, 27

Pelgrims V. et al., 2023, A&A, 670, A164

Quintana A. L., Wright N. J., Jeffries R. D., 2023, MNRAS, 522, 3124

Rautela B. S., Joshi G. C., Pandey J. C., 2004, Bull. Astron. Soc. India, 32, 159

Schubert E., Sander J., Ester M., Kriegel H. P., Xu X., 2017, ACM Trans. Database Syst. (TODS), 42, 1

Serkowski K., Mathewson D., Ford V., 1975, ApJ, 196, 261

Van Leeuwen F., 2007, A&A, 474, 653

Wang J.-W., Lai S.-P., Eswaraiah C., Clemens D. P., Chen W.-P., Pandey A. K., 2017, ApJ, 849, 157

Whittet D. C. B., 1992, J. British Astron. Assoc., 102, 175

Whittet D., 2004, in Witt A. N., Clayton G. C., Draine B. T., eds, ASP Conf. Ser. Vol. 309, Astrophysics of Dust. Astron. Soc. Pac., San Francisco, p. 65

Whittet D., Hough J., Lazarian A., Hoang T., 2008, ApJ, 674, 304

SUPPORTING INFORMATION

Supplementary data are available at *MNRAS* online.

Please note: Oxford University Press is not responsible for the content or functionality of any supporting materials supplied by the authors. Any queries (other than missing material) should be directed to the corresponding author for the article.

APPENDIX A: MODEL SELECTION OF TWO DUST LAYER MODEL USING BISP-1

To determine the number of dust layers along the LOS of six clusters, we used the BISP-1 package to fit the stellar polarization and parallax data with one-dust layer and two-dust layer models. The best model was chosen based on two criteria (i) model evidence returned by the nested sampling method from the dynesty sampler and (ii) akaike information criterion (AIC), which measures the information loss when the model is used to represent the data. The best model is the one with the highest model evidence and the lowest AIC value. From the model comparisons, BISP-1 predicted the two-layer model as a better model than that of the one-dust layer. We tried fitting the data with a three-layer model too, but the results were similar. So, we decided to go with the two-layer model.

This paper has been typeset from a TEX/LATEX file prepared by the author.